Acta Crystallographica Section A
Foundations of Crystallography
ISSN 0108-7673

Received 16 June 2010
Accepted 26 August 2010

© 2010 International Union of Crystallography
Printed in Singapore – all rights reserved

Simultaneous determination of highly precise Debye–Waller factors and structure factors for chemically ordered NiAl

X. H. Sang,* A. Kulovits and J. M. K. Wiezorek

Department of Materials Science and Mechanical Engineering, Swanson School of Engineering, University of Pittsburgh, 648 Benedum Hall, 3700 O'Hara Street, Pittsburgh, PA 15261, USA. Correspondence e-mail: xis20@pitt.edu

Accurate Debye–Waller (DW) factors and several low-index structure factors of chemically ordered β-NiAl at different temperatures have been measured using an off-zone-axis multi-beam convergent-beam electron diffraction method. The temperature dependences of DW factors of Ni and Al atoms are compared with previous experimental measurements and theoretical calculations. The temperature below which the DW factor of Ni becomes smaller than that of Al was found to be lower than previously reported. Structure factors are determined with an accuracy of 0.05% and compared with prior reports.

1. Introduction

Quantitative convergent-beam electron diffraction (QCBED) methods have been widely used to measure temperature factors, *i.e.* Debye–Waller (DW) factors, and structure factors of various structures (Tsuda & Tanaka, 1999; Zuo *et al.*, 1999; Ogata *et al.*, 2008; Jiang *et al.*, 2003). Unlike traditional X-ray diffraction (XRD) methods, for which accuracy is strongly influenced by the presence of crystalline defects in the sample, in CBED (convergent-beam electron diffraction) experiments this problem can be avoided because the electron beam interacts with very small sample volumes ($\sim$200 nm^3 for CBED samples compared to $\sim 2.7 \times 10^{16}$ nm^3 or 2.7×10^7 μm^3 for XRD samples). Additionally, careful selection and *in situ* transmission electron microscopy (TEM) analysis of the sample area can be used to ascertain that the investigated sample volume is defect free, which is impossible for XRD.

Traditionally, two different QCBED sample-to-beam orientations have been proposed. Zuo *et al.* (1999) and other researchers (Jiang *et al.*, 2003) use a systematic row method in which the sample is tilted such that only the transmitted beam and one diffracted beam are strongly excited. In this diffraction condition, a strong two-beam condition, the intensity in the CBED pattern is highly sensitive to changes in the structure factor of the excited diffracting systematic row reflection. In this method one-dimensional line profiles are compared with Bloch wave calculation results. While computation is relatively uncomplicated, a disadvantage of this method is that only one structure factor can be obtained from one experimental CBED pattern. Overcoming this limitation of the systematic row method, Saunders *et al.* (1995) used a zone-axis pattern (ZAP) method. A CBED pattern acquired in a zone-axis orientation is compared to the two-dimensional theoretical data of each disc. This method enables simultaneous determination of structure factors of many reflections of planes that are contained in the chosen zone axis. Historically this technique required disadvantageously long computation times. However, as computer technology has improved, in recent years the computation times for calculations and refinements of ZAP CBED patterns have been significantly reduced (Mueller *et al.*, 2009). For CBED pattern acquisition Tsuda & Tanaka (1999) used a transmission electron microscope equipped with an in-column energy filter, which is capable of recording diffraction intensities at high diffraction angles with small image distortions. Hence, they were able to include structure- and DW-factor-sensitive high-order Laue zone (HOLZ) discs in ZAP refinements, thereby improving the robustness of the computational refinements (Tsuda & Tanaka, 1999; Tsuda *et al.*, 2002; Ogata *et al.*, 2004).

Although QCBED methods have been used successfully in charge-density distribution determination for various materials in the past two decades, there are still limitations in the applicability of this method. For instance, it remains difficult to determine DW factors and structure factors by QCBED methods alone. In most previous reports on QCBED for electron-density studies, either structure factors were obtained from QCBED while using DW factors determined by X-ray diffraction (Zuo *et al.*, 1999; Jiang *et al.*, 2003) or DW factors were obtained from QCBED while using structure factors from first-principle calculations (Nüchter *et al.*, 1998*a*). Although simultaneous determination of DW and structure factors from one pattern was reported by Saunders *et al.* (1999*a*,*b*) using a ZAP method for Ni and Cu, its application to unknown structures has not been fully explored. Ogata *et al.* (2004, 2008) used the HOLZ ZAP method to simultaneously determine DW factors and structure factors for *h*-$BaTiO_3$ and Si. However, in order to apply the HOLZ ZAP CBED method it is necessary to use a TEM instrument equipped with an in-

column energy filter specifically modified for this purpose (Tanaka *et al.*, 1998), which is not readily available. More frequently, standard TEM instruments are equipped with a post-column energy filter, which typically limits the diffraction angle and therefore does not allow simultaneous acquisition of the ZOLZ (zero-order Laue zone) and HOLZ discs in ZAP CBED.

In Sang *et al.* (2010) we used an off-zone-axis multi-beam convergent-beam method to determine DW factors and structure factors of Si simultaneously. This method uses special off-zone-axis beam orientations where four or six reflections intersect the Ewald sphere or have excitation errors close to zero. Dynamic interactions among four or six excited beams ensure a high sensitivity of the CBED pattern intensity to changes in the respective structure factors and the DW factors. In this paper, we apply this method to investigate DW and structure factors of chemically ordered β-NiAl with the B2 (CsCl type) structure in *Strukturbericht* notation. β-NiAl is a simple cubic structure, which belongs to the space group $Pm3m$ (No. 221). The unit cell of β-NiAl contains one Ni atom at 0, 0, 0 and one Al atom at $\frac{1}{2},\frac{1}{2},\frac{1}{2}$ and has a lattice constant a = 2.8863 Å. In chemically ordered structures of metal species DW factors have to be determined for each atom species. The temperature dependence of DW factors of β-NiAl has been previously investigated theoretically by Gumbsch & Finnis (1996), and experimentally by Nüchter *et al.* (1998*a*,*b*) measuring CBED patterns at 110 K, and by XRD experiments at room temperature by Georgopoulos & Cohen (1977). The theoretical and combined experimental studies report that a cross-over temperature exists for β-NiAl, below which the amplitudes of thermal vibrations of Al exceed those of Ni, and above which the inverse holds, *i.e.* above the cross-over temperature the thermal vibration amplitude of Ni has been found to be larger than that of Al. The prior works of Gumbsch & Finnis (1996), Nüchter *et al.* (1998*a*) and Georgopoulos & Cohen (1977) determined the cross-over temperature at about 140 K. However, from Debye temperature data (Mostoller *et al.*, 1989) a cross-over temperature of 90 K can be deduced. We applied the highly accurate and robust off-zone-axis multi-beam CBED method to determine DW factors of β-NiAl for various temperatures ranging from room to liquid-nitrogen temperature. This CBED experimentation enabled a more accurate determination of the cross-over temperature, which we present and discuss in this study.

2. Experiments

2.1. Sample preparation

β-NiAl samples used for TEM investigation were obtained from an equiatomic composition β-NiAl single-crystal plate with [001] surface normal. The plate was first reduced to about 100 µm. From the plate discs with a diameter of 3 mm were obtained. The discs were reduced in thickness to about 50 µm. The 3 mm discs were electro-polished with a Fischione Model 140 using a solution of 5% perchloric acid and 95% ethanol at 243 K. Prior to each TEM session the electro-polished β-NiAl TEM samples were plasma-cleaned using a South Bay Technology 'PC 2000' Plasma Cleaner to remove carbonaceous contamination from the sample surface.

2.2. Experimental CBED and data pre-processing

Experimental CBED patterns were acquired using a Jeol JEM 2100 F transmission electron microscope operated at nominally 200 kV and equipped with a GIF TRIDIEM post-column energy filter (Gatan Inc.). A low-background, double-tilt cooling stage holder (Gatan Inc.) was used to acquire CBED patterns at temperatures as low as 100 K to reduce thermal diffuse scattering (TDS). Zero-loss peak, energy-filtered CBED patterns were acquired with a 5–8 eV-wide energy-selecting slit using an electron-beam diameter of 0.5 nm in order to eliminate thickness variations in the illuminated area that could give rise to intensity variations in the CBED pattern intensity. The CBED patterns were recorded on a charge-coupled device (CCD) camera with a maximum resolution of 2048 × 2048 and for sample temperatures of 100, 133 and 173 K and room temperature, 300 K.

Instead of Kikuchi lines, which were absent in the energy-filtered near-⟨100⟩ zone-axis CBED patterns even at sample thicknesses of 500 nm, we used features in each disc to determine the approximate beam–sample orientation. Discs with deviation vectors **s** close to or equal to zero were selected for refinement since the signal-to-noise ratio in those discs is satisfactory. Each point in the selected discs is associated with a beam direction, which is used to calculate a theoretical intensity based on Bloch wave methods (Bethe, 1928; Spence, 1993; Tsuda & Tanaka, 1995; Sang *et al.*, 2010). The experimental intensity of each point is directly extracted from the image file. As the background signal around discs is negligible, *i.e.* inelastic scattering is minimal, the background inside the discs is set to zero. Each disc contains at least 80 000 data points, which is sufficient to achieve accurate fitting results.

2.3. Refinement procedure

Refinements were performed by comparing intensity distributions of experimental CBED patterns with simulated CBED patterns. Intensity distributions in simulated patterns are calculated based on Bloch wave theory, which has been described in previous papers (Bethe, 1928; Spence, 1993; Tsuda & Tanaka, 1995; Sang *et al.*, 2010). The goal of the refinement is to minimize the objective function S, which measures the difference between the observed experimental intensity, $I_i^{\rm obs}$, and the calculated intensity, $I_i^{\rm cal}$, and is defined as

$$S = \sum_i (I_i^{\rm obs} - cI_i^{\rm cal})^2, \qquad (1)$$

with c the scale factor. The optimization is realized by variation of parameters that are used in the theoretical calculation, such as structure factors, sample thickness, sample surface orientation, accelerating voltage *etc.* Although DW factors $B_{\rm Ni}$

and $B_{\rm Al}$ are not directly included in the calculation, they are contained in structure factors F_{hkl} as follows:

$$F_{hkl} = f_{\rm Ni}\exp(-B_{\rm Ni}s^2) + (-1)^{h+k+l} f_{\rm Al}\exp(-B_{\rm Al}s^2), \qquad (2)$$

where s is $g_{hkl}/2$, and $f_{\rm Ni}$ and $f_{\rm Al}$ are atomic scattering factors. In this formulation the DW factors can be interpreted as dampening terms. During the refinement, several low-order structure factors are relaxed. Atomic scattering factors, based on data from Doyle & Turner (1968), are used as starting values, which are optimized during the refinement. DW factors and absorption are relaxed. For high-order structure factors only the DW factors are relaxed. Absorption factors and atomic scattering factors are fixed. Absorption factors are calculated with a method described by Bird & King (1990). This approximation is reasonable as atoms in high-index planes behave like free atoms. Only in low-index planes up to indices 200 do bonding effects cause significant deviations in the structure factor from the independent-atom model (IAM) (Lu *et al.*, 1992).

The goodness of fit (GOF) is evaluated using a weighted reliability factor (Tsuda & Tanaka, 1995),

$$R_{\rm w} = \left[\frac{\sum_i (I_i^{\rm obs} - cI_i^{\rm cal})^2/\sigma_i^2}{\sum_i (I_i^{\rm obs})^2/\sigma_i^2}\right]^2, \qquad (3)$$

with the standard deviation for the ith point, σ_i. Generally, $\sigma_i = (I_i^{\rm obs})^{1/2}$. Generally, a smaller $R_{\rm w}$ can be interpreted as a better correspondence of the observed with theoretically determined intensities, *i.e.* a smaller $R_{\rm w}$ corresponds to a better refinement. The perfect fit between the observed and the calculated CBED patterns would result in an $R_{\rm w}$ value that is zero, *i.e.* when $I_i^{\rm obs}$ is identical to $cI_i^{\rm cal}$.

3. Results

3.1. Orientation selection – sensitivity to structure factors

A beam–sample orientation that has high sensitivity to the DW factors and structure factors is essential for successful and robust simultaneous refinements of both factors. Four different orientations near the [001] zone axis were acquired and tested for stability of the refinements. The first beam–sample orientation is a zone-axis orientation (Fig. 1*a*). The second orientation (condition I) is a multi-beam near-zone-axis orientation, where the crystal is tilted such that the Ewald sphere intersects the transmitted beam and the reflections g_{100}, g_{110} and g_{010}, *i.e.* the transmitted beam and g_{100}, g_{110} and g_{010} are excited (Fig. 1*b*). The third orientation (condition II) is a multi-beam near-zone-axis orientation with an excited transmitted beam, and excited g_{110}, $g_{\bar{1}10}$ and g_{020} (Fig. 1*c*). Condition III is a multi-beam near-zone-axis orientation with an excited transmitted beam, and g_{200}, g_{020} and g_{220} excited (Fig. 1*d*). All test patterns were recorded at 100 K.

Fig. 2 shows the refinement results obtained from the patterns in Fig. 1. Fig. 2(*a*) shows the results for the zone-axis orientation in Fig. 1(*a*). For ZAP patterns, data points in the $0\bar{1}0$, 010, 000, $\bar{1}00$ and 100 discs are compared with the results of the Bloch wave calculation. Each disc contains 144 471 data points. Refinement of each pattern was implemented by relaxing the DW factors $B_{\rm Ni}$ and $B_{\rm Al}$, and the structure factors of reflections 100, 110 and 200. Reflections whose excitation errors are less than 0.06 Å^{-1} are used as exact beams in the Bloch wave calculation. Reflections whose excitation errors are between 0.06 and 0.09 Å^{-1} are included in the calculation using the Bethe approximation (Spence & Zuo, 1992). Approximately 145 exact beams and 75 Bethe beams are included, depending on slight changes in beam–sample orientation. This number of beams is too small for accurate refinements but sufficient to test the sensitivity of beam–sample orientations. For more accurate refinement of the DW factors and structure factors, many more beams (approximately 220 exact beams and 220 Bethe beams) are included in the refinement, which results in longer calculation times. Relaxation of higher reflections, such as 210, in the refinement does not improve the result. It increases the probability that the refinement result gets trapped in a local minimum rather than converging to the global minimum. The accelerating voltage was determined to be around 203 kV using the HOLZ lines method (Zuo, 1992). The thickness of the investigated area was determined as 146.6 nm.

Figs. 2(*b*), 2(*c*) and 2(*d*) show the results of the refinements for the multi-beam near-zone-axis conditions in Figs. 1(*b*), 1(*c*) and 1(*d*), respectively. The disc selection for multi-beam near-zone-axis conditions is straightforward. Discs that are intersected by the Ewald sphere should be included in the refinement as those beams interact strongly with the transmitted and the other diffracted beams with $\mathbf{s} \simeq 0$. Furthermore, the intensity in those discs is higher compared to discs with $\mathbf{s} \neq 0$.

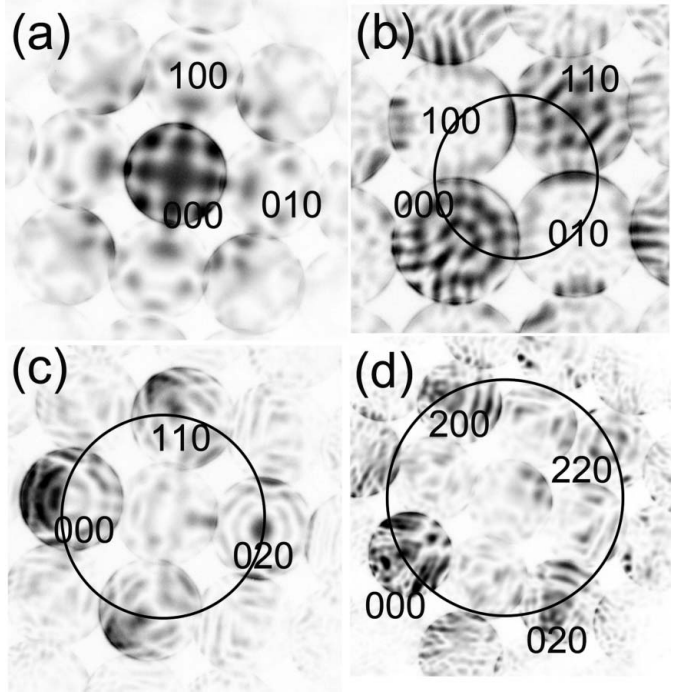

Figure 1
Inverted CBED patterns along different orientations. Black circles are traces of the Ewald sphere for each orientation.

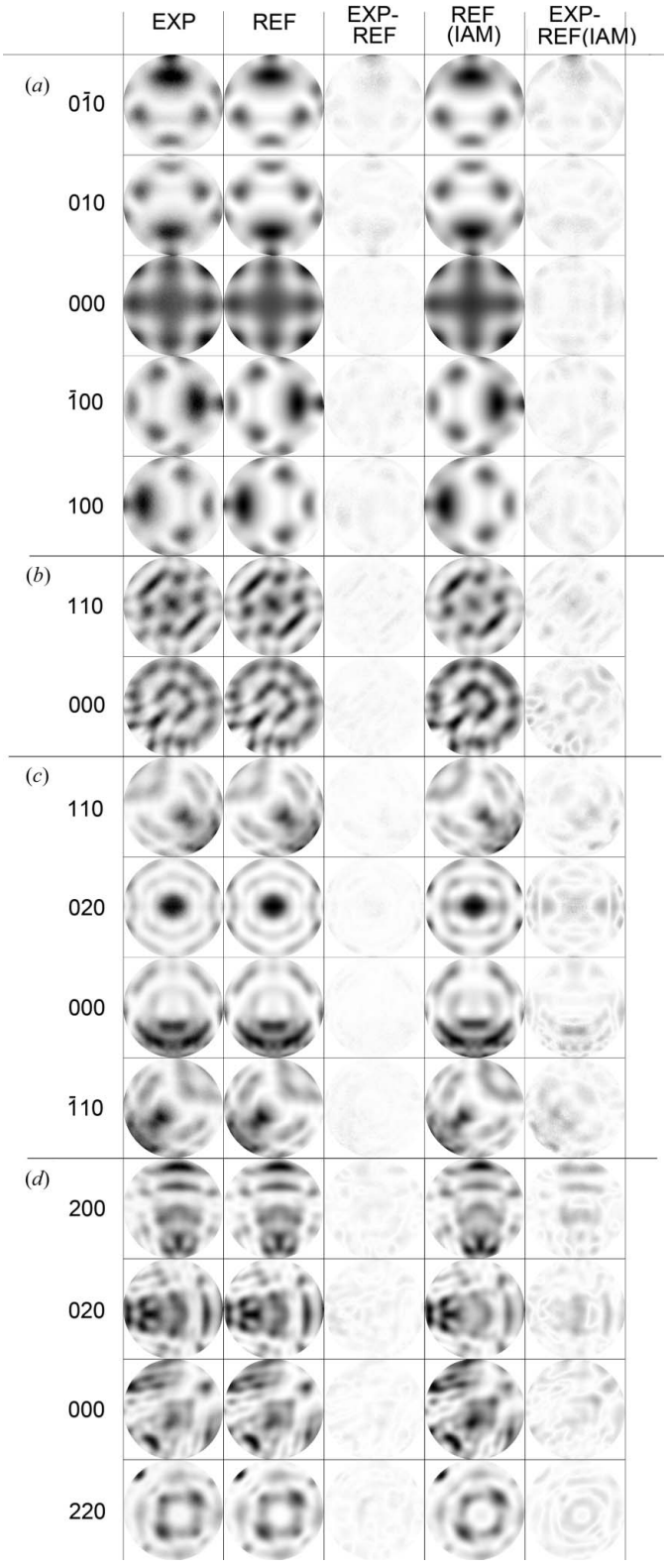

Figure 2
Refinement results of patterns recorded at different orientations. The first column in each part shows experimental discs. The second column shows calculated discs by relaxing the structure factors and DW factors. The fourth column shows calculated discs by only relaxing the DW factors and assuming the IAM. The third column and the fifth column show the absolute value of the deviation between column 1 and column 2, and between column 1 and column 4, respectively.

For condition I (Fig. 2*b*) data points in the 000 and 110 discs are used for comparison between the experimental data and simulated data. Each disc contains 202 055 data points. The 100 and 010 discs are not included as the signal-to-noise ratio in both discs is insufficient for accurate refinements. Patterns were refined by relaxing the DW factors $B_{\rm Ni}$ and $B_{\rm Al}$ and the structure factors of reflections 100, 110 and 200. The thickness of that area is 217.2 nm. For condition II (Fig. 2*c*) data points in the 000, $\bar{1}$10, 110 and 020 discs are included in the refinement. Each disc contains 138 143 data points. The DW factors $B_{\rm Ni}$ and $B_{\rm Al}$ and the structure factors of the 100, 110 and 200 reflections are relaxed during refinement. The thickness of that area is 207.7 nm. For condition III (Fig. 2*d*), data points in the 000, 200, 020 and 220 discs are used in the refinement. Each disc contains 87 811 data points. The DW factors $B_{\rm Ni}$ and $B_{\rm Al}$ and the structure factors of reflections 100, 110, 200, 220 and 310 are relaxed during refinement. The thickness of that area has been determined as 173.2 nm.

In Fig. 2 the index column shows the **g** vectors of the discs displayed in the following columns. The first column in Fig. 2 shows the intensity distribution of the **g** discs corresponding to the respective **g** vectors indicated in the index column. The second and fourth columns in Fig. 2 show the calculated intensities of the respective **g** discs using refinement-optimized DW and structure factors and the calculated intensities using the independent atom model (IAM), respectively. The comparison with the IAM simulations was included in this figure to illustrate the effect of bonding on the intensity distribution in the experimentally acquired and refined discs. The third and fifth columns of Fig. 2 show the absolute deviations of intensities in the experimental and the refined discs and experimental and IAM-based disc intensities, respectively. Comparison of columns three with five shows a vast improvement in the CBED intensity matching when using the optimized DW and structure factors instead of using the IAM values. The discs in column three in Figs. 2(*b*) and 2(*c*) are almost featureless, exhibiting nearly uniform white contrast after the refinement, whereas little improvement can be seen in Fig. 2(*a*). This improvement is also reflected in changes in the $R_{\rm w}$ values. The $R_{\rm w}$ values for calculations based on the IAM model for the different crystal orientations and CBED methods are (*a*) 0.186, (*b*) 0.232, (*c*) 0.364 and (*d*) 0.296. After structure-factor refinement the $R_{\rm w}$ values improve to 0.150, 0.110, 0.136 and 0.154, respectively. The smallest improvement was achieved in the zone-axis orientation (Fig. 2*a*), while the orientation in condition II (Fig. 2*c*) showed the biggest improvement. Hence, condition II is most sensitive to changes in structure factors. Condition III shows the least improvement among the multi-beam near-zone-axis conditions. This orientation is furthest away from a true zone-axis orientation. While the IAM approximation of the atomic scattering factors is better compared to the conditions I and II, the combination of finer and more numerous features (Fig. 2*d*) with the actual disc size leads to complications in disc misalignment for data extraction, thereby degrading the refinement result. Nevertheless, condition III still yields better improvements than the zone-axis orientation. Hence, among

Table 1
Refined DW factors and corresponding R_w values (test case) from patterns of different sample–beam orientations.

	Zone-axis pattern			Condition I			Condition II			Condition III		
No.	B_{Ni} (Å^2)	B_{Al} (Å^2)	R_w	B_{Ni} (Å^2)	B_{Al} (Å^2)	R_w	B_{Ni} (Å^2)	B_{Al} (Å^2)	R_w	B_{Ni} (Å^2)	B_{Al} (Å^2)	R_w
1	0.1948	0.1665	0.21	0.2174	0.1971	0.14	0.2161	0.2667	0.18	0.2298	0.2431	0.18
2	0.3028	0.2374	0.15	0.2268	0.2250	0.12	0.1942	0.2187	0.16	0.2393	0.2353	0.19
3	0.2126	0.2136	0.20	0.2135	0.2001	0.11	0.2371	0.2262	0.17	0.1993	0.3056	0.17
4				0.1982	0.2051	0.10	0.2135	0.2163	0.14	0.1783	0.2291	0.15
5				0.2042	0.2509	0.17	0.2196	0.2040	0.15	0.1884	0.2605	0.17
6				0.1857	0.2481	0.17	0.2225	0.2343	0.15	0.2131	0.2563	0.17
Average	0.2367	0.2058		0.2076	0.2210		0.2172	0.2277		0.2080	0.2550	
Standard deviation	0.0579	0.0361		0.0147	0.0241		0.0139	0.0216		0.0238	0.0275	

the four probed orientations the zone-axis orientation (Figs. 1*a* and 2*a*) is the least sensitive to changes in the structure factor.

3.2. Orientation selection – sensitivity to DW factors

If a beam–sample orientation is sensitive to changes in the DW factors, the optimized DW factors obtained from different patterns should result in the same values, within the error bars, independently of orientation and thickness. We refined here three different zone-axis orientations, and for six different condition-I, six different condition-II and six different condition-III patterns, each acquired from different sample thicknesses. For each CBED condition, the DW factors and corresponding low-index structure factors as described above were included in the refinement. For the refinements we used the same parameters as described in §3.1, which is sufficient for beam sensitivity determination and maintenance of a high computation speed. The results from the refinements of those patterns are listed in Table 1.

Table 1 indicates that the DW factors determined from zone-axis patterns are the most inconsistent. The three data points show big scatter, which results in high standard deviations for B_{Ni} and B_{Al}. This is consistent with the fact that the zone-axis pattern exhibits the least sensitivity to changes in structure factors (Fig. 2*a*), as a relaxation of the DW factors in the refinement actually changes the high-index structure factors. Refinements of patterns obtained in conditions I and II result in DW factors with relatively small standard deviations. The slightly higher standard deviations obtained from condition III render this condition less suitable than condition II. Additionally, in condition II, all the four discs that intersect the Ewald sphere exhibit fine feature details and a good signal-to-noise ratio, which are optimal for data extraction. Conversely, in condition I, the intensities of the 100 and 010 discs are very low and strongly affected by noise, rendering both discs unsuitable for inclusion in refinement. Hence, condition I provides a much smaller number of usable data points than condition II, resulting in improved stability of the refinement using condition II. Since condition II provides the best combination of sensitivity to structure factors and DW factors and robustness of the refinements, it was used predominantly for the simultaneous accurate determination of structure and DW factors.

3.3. Temperature dependence of DW factors of β-NiAl

Multi-beam near-zone-axis CBED patterns acquired in condition II were obtained at 100, 133, 173 and 300 K. For each pattern, data points in the 000, $\bar{1}10$, 110 and 020 discs were included in the refinement. The DW factors B_{Ni} and B_{Al} and structure factors of reflections 100, 110 and 200 were relaxed during refinement. Other beams that have excitation errors less than 0.09 Å^{-1} are used as exact beams in the Bloch wave calculation. Beams whose excitation errors are between 0.09 and 0.2 Å^{-1} are included in the calculation using the Bethe approximation (Spence & Zuo, 1992). Approximately 220 exact beams and 220 Bethe beams are included depending on slight changes of beam–sample orientations. Based on a convergence test, this number of beams has proved sufficient to avoid error caused by truncation.

The optimized DW factors B_{Ni} and B_{Al} *versus* sample thickness at 100, 133, 173 and 300 K are plotted in Figs. 3(*a*), 3(*b*), 3(*c*) and 3(*d*), respectively. Figs. 3(*a*), 3(*b*), 3(*c*) and 3(*d*) include the refinement results from 16, 21, 22 and 5 patterns obtained for different sample thicknesses, respectively. All refinement results have an R_w value better than 0.2. Refinements that yield R_w values larger than 0.2 are generally unreliable and would result in significant deviations of the experimental pattern from the calculated pattern. Although many patterns obtained at room temperature have been refined, only five of them yielded R_w values smaller than 0.2 (Fig. 3*d*), which can be attributed mostly to increasing detrimental effects from TDS contributions. For patterns acquired at lower temperatures, R_w values are typically near 0.15. The reduced contribution from TDS greatly improves the image quality and refinement reliability.

The average values and standard deviations of B_{Ni} and B_{Al} calculated from data points in Fig. 3 are summarized in Table 2, which shows increasing scatter as the temperature increases, consistent with the detrimental effects from TDS. Fig. 3 and Table 2 show that as the temperature increases, B_{Ni} increases more rapidly than B_{Al} in this temperature range. At 100 K (Fig. 3*a*), the averaged B_{Ni} is only slightly larger than B_{Al} and for some data points B_{Al} is larger than B_{Ni}. At 100 K the temperature factors for Ni and Al are indistinguishable within the error of one standard deviation. At 133 K and higher temperatures B_{Ni} is larger than B_{Al}, significantly so at room temperature (Fig. 3*d*).

Table 2
DW factors of β-NiAl at 100, 133, 173 and 300 K.

Temperature (K)	B_{Ni} (Å^2)	Standard deviation (Å^2)	B_{Al} (Å^2)	Standard deviation (Å^2)
100	0.2462	0.0103	0.2265	0.0132
133	0.2969	0.0112	0.2591	0.0145
173	0.3475	0.0194	0.2867	0.0186
300	0.5205	0.0364	0.4437	0.0228

3.4. Structure factors of β-NiAl at various temperatures

Along with the DW factors obtained from the refinements described above, electron structure factors for the 100, 110 and 200 reflections are also determined simultaneously. In our algorithm (Bloch wave calculation), we relaxed the DW factors of Ni and Al and several low-order electron structure factors simultaneously. High-order X-ray structure factors were approximated by the independent atom model and were fixed. High-order electron structure factors were obtained from conversion of the fixed X-ray structure factors and the 'to be refined' Debye–Waller factors using the Mott formula (Spence & Zuo, 1992). After completion of the refinement, low-order X-ray structure factors were calculated from refined low-order electron structure factors using the refined DW factors. One typical refinement result is shown in Fig. 4, which plots $F_g(100)$ and $F_g(110)$ *versus* sample thickness from patterns obtained at 133 K. Consistent structure factors are refined from patterns acquired in a thickness range of 240–400 nm.

The average values and standard deviations of low-index structure factors are summarized in Table 3. Despite simultaneously refining for DW factors and structure factors, the resulting refined structure factors are still highly accurate. The standard deviation for $F_g(100)$ and $F_g(110)$ at 100 K is close to 0.05%. Standard deviations of the measurements for $F_g(100)$ at all temperatures are less than 0.1%. The structure factors decrease as the temperature increases because of larger atomic vibration amplitudes at higher temperatures (Table 3). Standard deviations generally increase as the temperature increases because inelastic scattering is more pronounced at higher temperatures. Additionally, carbonaceous contamination films can grow rapidly under the electron beam illumination at room temperature for longer acquisition times, which can lead to increased background noise. At lower temperatures ($T \leq 173$ K), hardly any carbonaceous film growth was observed.

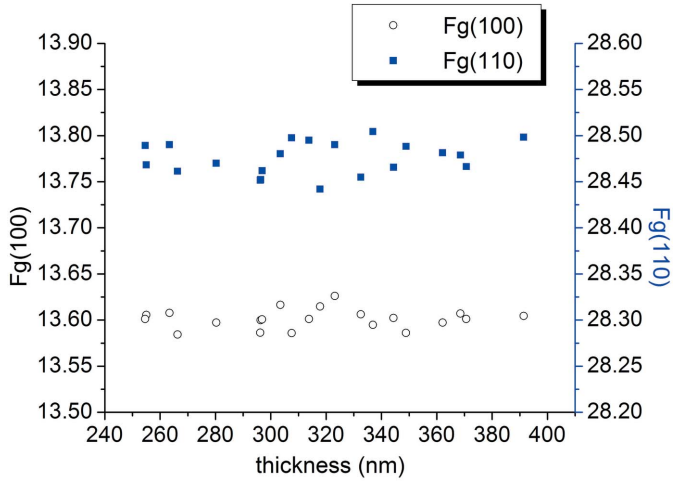

Figure 4
Refined structure factors *versus* thickness at 133 K [left axis: $F_g(100)$; right axis: $F_g(110)$].

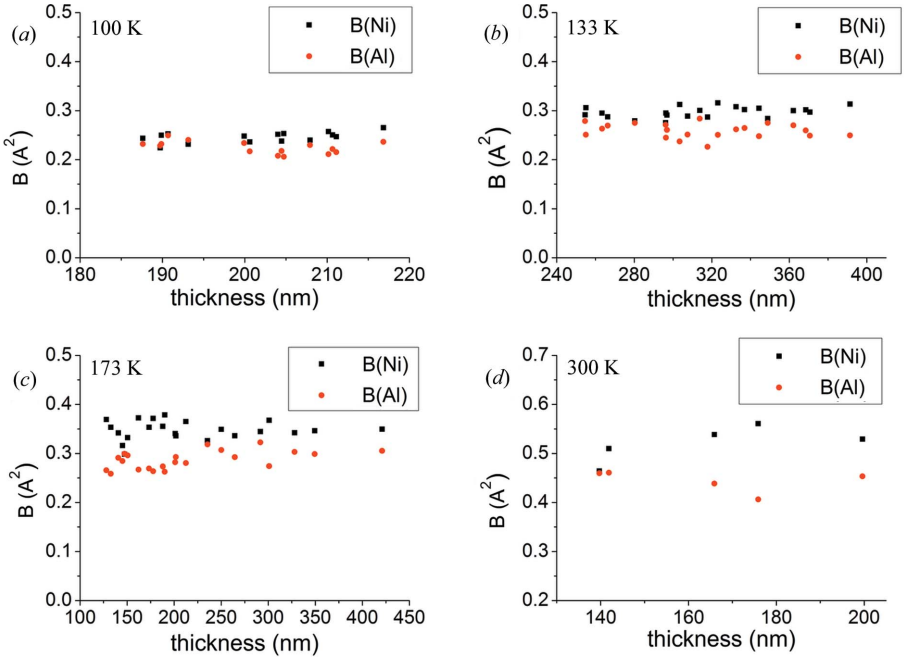

Figure 3
Refined DW factors *versus* thickness at different temperatures.

4. Discussion

4.1. Comparison of DW factors with previous results

Several different groups have previously determined the DW factors and structure factors of β-NiAl using various methods. Georgopoulos & Cohen (1977) determined the DW factor amplitudes for Ni and Al, B_{Ni} = 0.51 Å^2 and B_{Al} = 0.47 Å^2, at room temperature using XRD. Nüchter *et al.* (1998*a*) used the systematic row CBED method at 100 K and obtained a mean thermal displacement of μ(Ni) = 0.55 pm and μ(Al) = 0.57 pm, which can be converted to B_{Ni} = 0.238 Å^2 and B_{Al} = 0.252 Å^2 using $B = 8\pi^2\langle\mu\rangle^2$. Both data sets agree acceptably well with our results for room temperature and 100 K. Our data differ from data reported by Nüchter *et al.* (1998*a*). In our case B_{Ni} is

Table 3
Low-index X-ray structure factors and absorption factors of β-NiAl at 100, 133, 173 and 300 K.

	100 K		133 K		173 K		300 K	
	Exp.	Std dev.	Exp.	Std dev.	Exp.	Std dev.	Exp.	Std dev.
$F_g(100)$	13.615	0.008	13.601	0.011	13.568	0.013	13.517	0.011
$F_g(110)$	28.564	0.016	28.476	0.018	28.383	0.022	28.081	0.046
$F_g(200)$	23.843	0.069	23.668	0.085	23.597	0.164	23.082	0.181
$F_{abs}(100)$	0.077	0.004	0.086	0.002	0.092	0.006	0.119	0.004
$F_{abs}(110)$	0.129	0.005	0.141	0.003	0.162	0.015	0.195	0.005
$F_{abs}(200)$	0.115	0.013	0.122	0.007	0.143	0.027	0.170	0.032

Table 4
Comparison of structure factors of reflections 100, 110 and 200 at room temperature, 300 K.

	Present result	Theory (LDA)†	Experiment‡	Experiment§	IAM¶
$F_g(100)$	13.517	13.45	13.53	13.47	13.270
$F_g(110)$	28.081	28.07	28.08	28.08	28.248
$F_g(200)$	23.082	22.99	22.60	23.02	23.120

† Lu *et al.* (1992). ‡ Fox & Tabbernor (1991). § Fox (1995). ¶ Doyle & Turner (1968).

higher than B_{Al}, while B_{Ni} is lower than B_{Al} in Nüchter's data at nominally the same temperature of 100 K. However, the average values in Nüchter's data are within the standard deviation B_{Ni} = 0.238 (30) and B_{Al} = 0.252 (25) (Nüchter *et al.*, 1998*a*) consistent with our results B_{Ni} = 0.246 (10) and B_{Al} = 0.226 (13). It should be noted that the standard deviation is smaller by a factor of 2–3 for the data presented here, *i.e.* the implementation of the multi-beam near-zone-axis method yields more accurate results than prior experimental reports.

4.2. Comparison of structure factors with previous results

Menon & Fox (1996) determined the structure factors and DW factors of β-NiAl using X-ray diffraction. More accurate results were obtained by Fox (1995) using the critical voltage method. Lu *et al.* (1992) calculated theoretical structure factors at 0 K and room temperature. The room-temperature data (300 K) from prior studies are compiled and compared with the presented results in Table 4. Additionally, Nüchter *et al.* (1998*b*) performed CBED measurements of six low-order structure factors using two-beam conditions at 110 K. The structure factors determined here at 100 and 133 K (Table 3) agree within the measurement uncertainty with values reported by Nüchter *et al.* (1998*b*). Our results are consistent with both other measurements and calculations.

4.3. Temperature dependence of DW factors

The temperature dependence of the DW factors of β-NiAl have been investigated previously by Gumbsch & Finnis (1996) using a direct real-space numerical simulation. Gumbsch & Finnis (1996) found that B_{Ni} is higher than B_{Al} at high temperature but lower than B_{Al} at low temperature. A cross-over temperature was determined to be around 140 K. The physical reason for a cross-over temperature is due to the fact that Ni has a higher atomic mass, which results in B_{Ni} being smaller than B_{Al} at lower temperatures. However, the temperature dependence of lattice vibration calculations for B2 ordered NiAl shows that B_{Ni} increases faster than B_{Al} as the temperature increases, which is reflected in a lower Debye temperature for Ni, Θ_{Ni}, than for Al, Θ_{Al} (Mostoller *et al.*, 1989; Gumbsch & Finnis, 1996).

From our QCBED result, B_{Ni} = 0.2969 (112) Å^2 and B_{Al} = 0.2591 (145) Å^2, at 133 K. Therefore, even taking into account the standard deviation, B_{Ni} is larger than B_{Al} (Fig. 3*b*). Furthermore, our measurements suggest that even at 100 K still B_{Ni} is larger than B_{Al}. However, the measured values for B_{Ni} and B_{Al} could be the same at 100 K, when the standard deviation of our measurements is considered. Our measurements imply that the cross-over temperature, below which B_{Al} is larger than B_{Ni}, is about 100 K or slightly less. We used the Einstein model and the Debye model to further analyze the cross-over temperature. The DW factor amplitude of an atom in a crystal can be related to the thermal vibration frequency distribution function $g(\omega)$ using the following equation (Willis & Pryor, 1975; Gumbsch & Finnis, 1996),

$$B = \frac{8\pi^2}{3mN_0}\int_0^\infty \frac{E(\omega)}{\omega^2} g(\omega)\,\mathrm{d}\omega, \qquad (4)$$

where $E(\omega) = 1/2(\hbar\omega) + \{(\hbar\omega)/[\exp(\hbar\omega/k_B^T - 1)]\}$, m is the atomic mass and N_0 is the number of atoms in the crystal. $g(\omega)$ must satisfy $3N_0 = \int g(\omega)\,\mathrm{d}\omega$. In the Einstein model, each atom oscillates independently and with the same frequency, which gives $g(\omega) = 3N_0\delta(\omega - \omega_E)$. In the Debye model, the vibration characteristics differ for frequencies below and above the Debye cut-off frequency, ω_D, such that $g(\omega) = 9N_0(\omega^2/\omega_D^3)$ for $\omega < \omega_D$ and 0 for $\omega > \omega_D$, which is related to the Debye temperature Θ_D by $\hbar\omega_D = k_B\Theta_D$. Based on these two different models, Einstein frequencies for the two atom species, ω_E(Ni) and ω_E(Al), and Debye temperatures, Θ_{Ni} and Θ_{Al}, can be optimized to fit the temperature dependence of the DW-factor-related vibration amplitudes measured here from the presented CBED data.

Einstein frequencies of ω_E(Ni) = 24.6 ps^{-1} and ω_E(Al) = 42.8 ps^{-1} result in the best comparison with the DW factor amplitudes obtained at the various temperatures in our experiments. Fig. 5(*a*) shows the temperature dependence of calculated B_{Ni} and B_{Al} values based on the Einstein model. The theoretical values show excellent consistency with our data at different temperatures, especially for B_{Al}. A cross-over temperature of 97.8 K is predicted by the Einstein model. Gumbsch & Finnis (1996) obtained ω_E(Ni) = 26.1 ps^{-1} and ω_E(Al) = 41.1 ps^{-1} using B_{Ni} and B_{Al} at room temperature from Georgopoulos & Cohen (1977). Both values agree fairly well with our calculation.

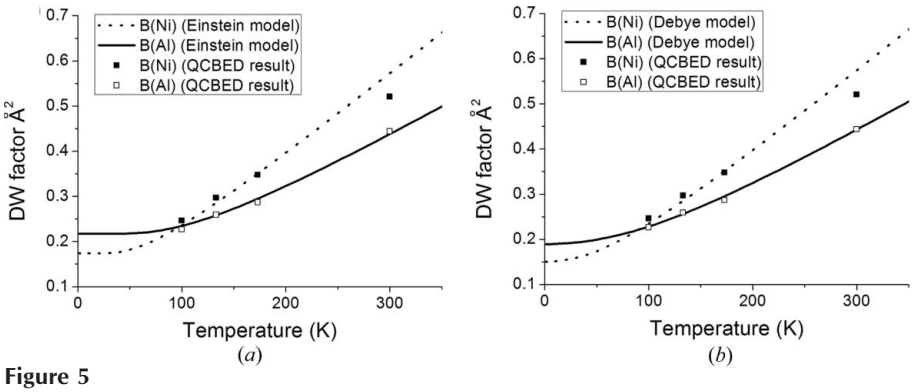

Figure 5
Plots of theoretical and experimental B_{Ni} and B_{Al} values *versus* temperature. (*a*) Einstein model, (*b*) Debye model.

When the Debye model is used, the best comparison between theoretical prediction and the CBED-based experimental measurements is achieved for Θ_{Ni} = 325 K and Θ_{Al} = 562 K. The temperature dependence of B_{Ni} and B_{Al} based on the Debye model is shown in Fig. 5(*b*). Again, good consistency is shown between theoretical calculation and experimental measurement, resulting in a cross-over temperature of 90.6 K. Θ_{Ni} and Θ_{Al} were determined by Mostoller *et al.* (1989) as 332 and 563 K using neutron scattering. Both Debye temperature values agree well with the calculation based on the CBED measurements presented here. Since the Debye model describes the temperature dependence of vibrations of crystalline structures more realistically than the Einstein model, the cross-over temperature predicted by the Debye model is considered more accurate. Nüchter *et al.* (1998*a*) estimated that electron-beam heating may increase the sample temperature by about $\Delta T \simeq 7$ K. The beam-heating effect may systematically shift the temperatures we report to higher values. The cross-over temperature is 90.6 (+7.0) K based on our experimental measurements by CBED, which is significantly lower than previously reported (Gumbsch & Finnis, 1996).

4.4. Advantage of using the multi-beam off-zone-axis condition

The multi-beam near-zone-axis CBED proposed by Sang *et al.* (2010) for the simultaneous refinements of precise Debye–Waller factors and structure factors was successfully tested on silicon. In the case of Si this method showed higher sensitivity and ensured more robust refinement results than CBED methods used previously. Here, we applied this method to the investigation of a more complex, chemically ordered binary B2 structure of NiAl, characterized by separate DW factors for the different atom species. Table 1 shows that the traditional zone-axis CBED method could not yield sufficiently accurate DW factors. Sang *et al.* (2010) showed that the systematic row method is not sufficiently accurate either, which is also reflected in Nüchter *et al.* (1998*a*). The robustness of multi-beam near-zone-axis-condition CBED is founded on the enhanced dynamic interaction between multiple different beams that are tilted exactly to or very close to their respective Bragg condition. These strong dynamical interactions distribute intensity more uniformly into each CBED disc and render the experimental data more robust against deterioration from noise and associated non-systematic errors.

5. Conclusion

Highly accurate structure factors and DW factors were simultaneously measured using a multi-beam near-zone-axis CBED method for B2 NiAl at different temperatures. An orientation close to a [001] zone-axis orientation was obtained by tilting the sample to bring the 200, 020 and 220 reflections into Bragg condition. In this orientation we obtained CBED patterns that produce robust DW factors and structure factors with an accuracy of 0.05% for F_g(100) and F_g(110) at 100 K. This study demonstrated the superior sensitivity of these types of multi-beam near-zone-axis orientations to changes of DW and structure factors relative to that of a [001] zone-axis orientation. The successful application of the refinements of special orientation QCBED patterns to the determination of DW factors and low-index structure factors of B2 NiAl suggests that the same method will be applicable to other complicated non-cubic metallic bonding systems with anisotropic DW factors, such as the tetragonal Cu–Au–I-type structures.

The temperature dependence of DW factors for the Ni and Al atoms in NiAl is explained using an Einstein model and a Debye model. Our CBED-based measurements qualitatively confirm prior studies by Gumbsch & Finnis (1996) which predicted that a cross-over temperature exists, at which Al and Ni would have the same DW factors. From the QCBED data presented in this study a more accurate and lower temperature of 90.6 K has been determined for this cross-over temperature.

This work was supported by a grant from the Office of Basic Energy Sciences, a division of Materials Science and Engineering, of the US DOE (grant No. DE-FG02-08ER46545).

References

Bethe, H. (1928). *Ann. Phys. Berlin*, **392**, 55–129.
Bird, D. M. & King, Q. A. (1990). *Acta Cryst.* A**46**, 202–208.
Doyle, P. A. & Turner, P. S. (1968). *Acta Cryst.* A**24**, 390–397.
Fox, A. G. (1995). *Scr. Metall. Mater.* **32**, 343–347.
Fox, A. G. & Tabbernor, M. A. (1991). *Acta Metall. Mater.* **39**, 669–678.
Georgopoulos, P. & Cohen, J. B. (1977). *Scr. Metall.* **11**, 147–150.
Gumbsch, P. & Finnis, M. W. (1996). *Philos. Mag. Lett.* **73**, 137–144.
Jiang, B., Zuo, J. M., Jiang, N., O'Keeffe, M. & Spence, J. C. H. (2003). *Acta Cryst.* A**59**, 341–350.
Lu, Z. W., Wei, S. H. & Zunger, A. (1992). *Acta Metall. Mater.* **40**, 2155–2165.
Menon, E. S. K. & Fox, A. G. (1996). *Acta Mater.* **44**, 2547–2555.
Mostoller, M., Nicklow, R. M., Zehner, D. M., Lui, S. C., Mundenar, J. M. & Plummer, E. W. (1989). *Phys. Rev. B*, **40**, 2856–2872.

Mueller, K., Schowalter, M., Jansen, J., Tsuda, K., Titantah, J., Lamoen, D. & Rosenauer, A. (2009). *Ultramicroscopy*, **109**, 802–814.
Nüchter, W., Weickenmeier, A. L. & Mayer, J. (1998*a*). *Acta Cryst.* A**54**, 147–157.
Nüchter, W., Weickenmeier, A. L. & Mayer, J. (1998*b*). *Phys. Status Solidi A*, **166**, 367–379.
Ogata, Y., Tsuda, K., Akishige, Y. & Tanaka, M. (2004). *Acta Cryst.* A**60**, 525–531.
Ogata, Y., Tsuda, K. & Tanaka, M. (2008). *Acta Cryst.* A**64**, 587–597.
Sang, X. H., Kulovits, A. & Wiezorek, J. M. K. (2010). *Acta Cryst.* A**66**, 685–693.
Saunders, M., Bird, D. M., Zaluzec, N. J., Burgess, W. G., Preston, A. R. & Humphreys, C. J. (1995). *Ultramicroscopy*, **60**, 311–323.
Saunders, M., Fox, A. G. & Midgley, P. A. (1999*a*). *Acta Cryst.* A**55**, 471–479.
Saunders, M., Fox, A. G. & Midgley, P. A. (1999*b*). *Acta Cryst.* A**55**, 480–488.
Spence, J. C. H. (1993). *Acta Cryst.* A**49**, 231–260.
Spence, J. C. H. & Zuo, J. M. (1992). *Electron Microdiffraction.* New York: Plenum Press.
Tanaka, M., Tsuda, K., Terauchi, M., Tsuno, K., Kaneyama, T., Honda, T. & Ishida, M. (1998). *J. Microsc.* **194**, 219–227.
Tsuda, K., Ogata, Y., Takagi, K., Hashimoto, T. & Tanaka, M. (2002). *Acta Cryst.* A**58**, 514–525.
Tsuda, K. & Tanaka, M. (1995). *Acta Cryst.* A**51**, 7–19.
Tsuda, K. & Tanaka, M. (1999). *Acta Cryst.* A**55**, 939–954.
Willis, B. T. M. & Pryor, A. W. (1975). *Thermal Vibrations in Crystallography*. London: Cambridge University Press.
Zuo, J. M. (1992). *Ultramicroscopy*, **41**, 211–223.
Zuo, J. M., Kim, M., O'Keeffe, M. & Spence, J. C. H. (1999). *Nature* (*London*), **401**, 49–52.